INORGANIC CHEMISTRY







FRONTIERS

RESEARCH ARTICLE

View Article Online
View Journal | View Issue



Cite this: *Inorg. Chem. Front.*, 2022, **9**, 4695

Simultaneous enhancement of near infrared luminescence and stability of Cs₂AgInCl₆:Cr³⁺ double perovskite single crystals enabled by a Yb³⁺ dopant†

Daiwen Chen,^a Xinguo Zhang,^b Jianwu Wei,^a Liya Zhou, ^D ^a Peican Chen,^a Qi Pang ^D * ^a and Jin Zhong Zhang ^D * ^c

Broadband near infrared (NIR) emission materials are of interest for various applications including non-destructive biomedical imaging. In this work, ytterbium ions (Yb³+) were successfully doped into $Cs_2AgInCl_6:Cr^3+$ (CAIC:Cr³+) double perovskite single crystals (DPSCs) by a facile hydrothermal method. Under 365 nm excitation, the co-doped CAIC:Cr³+,Yb³+ DPSCs showed broad NIR emission ranging from 800 to 1400 nm, which spanned the NIR-I (700–900 nm) and NIR-II (1000–1700 nm) bio-windows, with an emission band at 1000 nm and a full-width at half maximum (FWHM) of 188 nm. It is found that Yb³+ ion doping could effectively improve the photoluminescence (PL) performance of CAIC:Cr³+ DPSCs. Compared to the photoluminescence quantum yield (PLQY) of 22.5% for the single doped CAIC:Cr³+, the co-doped CAIC:Cr³+,Yb³+ DPSCs show a higher PLQY of ~45%, which is attributed to the synergistic effect of reduced non-radiative recombination due to defect passivation and increase in crystallinity, and energy transfer (ET) of self-trapped excitons (STEs) to Cr^3+ . As a demonstration of applications, NIR pc-LEDs were fabricated by combining the as-synthesized NIR-emitting phosphor CAIC:Cr³+,Yb³+ with InGaN UV chips (λ_{em} = 365 nm) and used to image veins in a palm and for night vision using a NIR camera. The results suggest that the synthesized CAIC:Cr³+,Yb³+ DPSCs have great potential in biological applications.

Received 21st May 2022, Accepted 15th July 2022 DOI: 10.1039/d2qi01104b

rsc.li/frontiers-inorganic

^aSchool of Chemistry and Chemical Engineering, Guangxi University/Key Laboratory of Electrochemical Energy Materials, Guangxi University, Nanning 530004, Guangxi, Peoples R China. E-mail: pqigx@163.com

1. Introduction

High efficiency broadband near infrared (NIR) light emitters are of strong interest for applications such as night vision and biomedical imaging due to the deep penetration of biological tissues and low damage to the human body. 1,2 Lead halide perovskites (APbX₃, A = Cs, CH₃NH₃, X = Cl, Br, I) have demonstrated promising applications in solar cells, photodetectors, light emitting diodes (LEDs), and other optoelectronic applications due to their superior photoelectric properties.3-5 However, they face obstacles for commercialization due to the toxicity of lead (Pb) and low stability against humidity, oxygen and light. 4-6 For this reason, low toxicity and high stability lead-free perovskite materials have attracted substantial attention. One strategy is to replace every two Pb toxicity cations with one monovalent cation and one trivalent cation, forming double perovskites (DPs) with the general formula A2B(I)B(III) X₆.8-15 Cs₂AgInCl₆ as one of the direct bandgap DPs with an optical bandgap (E_{σ} OPT) of ~3.3 eV has attracted much attention recently. Pure and modified Cs₂AgInCl₆ with excellent moisture, light and heat stability offers a promising alternative to Pb-based halide perovskites. Previous research on the

^bSchool of Pharmaceutical Sciences, Southern Medical University, Guangzhou 510515. Peoples R China

^cDepartment of Chemistry and Biochemistry, University of California, Santa Cruz, California 95064, USA. E-mail: zhang@ucsc.edu

[†] Electronic supplementary information (ESI) available: Experimental sections; XRD patterns of CAIC:x%Cr (x=0, 10, 20, 30, 40, 50) DPSCs; XRD patterns of CAIC:30%Cr,y%Yb (y=0, 1, 2, 3) DPSCs; SEM image and EDS spectra of CAIC:30%Cr with the corresponding atomic maps; PLE spectra of CAIC:30%Cr with the corresponding atomic maps; PLE spectra of CAIC:30%Cr $^{3+}$,y%Yb $^{3+}$ (y=0, 1, 2, 3); PL spectra of CAIC:30%Cr $^{3+}$,y%Yb $^{3+}$ (y=0, 1, 2, 3). The incorporated samples were tested at $\lambda_{\rm ex}=365$ nm; excitation-wavelength-dependent (320–600 nm) PL spectra of CAIC:30%Cr $^{3+}$,3%Yb $^{3+}$; PL spectra of CAIC:30%Cr $^{3+}$,3%Yb $^{3+}$ and CAIC:Yb $^{3+}$. The emission spectrum of CAIC:Yb $^{3+}$ in the figure is magnified tenfold; PL curves measured from CAIC:Cr $^{3+}$ and CAIC: Ln $^{3+}$ samples; TRPL decay curves of CAIC:Cr $^{3+}$ doped with or without Ln $^{3+}$ ions; details of X-ray crystallographic parameters of single crystals; details of atom occupation situation of Cs₂AgIn_{0.7}Cr_{0.3}Cl₆ single crystals; Cr $^{3+}$ and Yb $^{3+}$ content from starting materials and measured by ICP. See DOI: https://doi.org/10.1039/d2qi01104b

luminescence of DPs has mainly focused on visible light emission. Mahor *et al.* first obtained a NIR phosphor *via* doping Yb³⁺ ions into Cs₂AgInCl₆. Nag *et al.* reported the Cs₂AgInCl₆ system co-doped with Bi and Er. Under 370 nm excitation, the emission intensity of the co-doped sample at 1540 nm was 45 times higher than that of the Er³⁺ doped sample. However, all these research studies focus on narrowband NIR emission and the PLQY still needs improvement. Therefore, exploring suitable strategies for broadband NIR emission and enhancing the PLQY is urgently needed.

Recently, there has been growing interest in novel phosphors doped with transition metal ions or trivalent lanthanide (Ln³⁺) ions. 18 For instance, the luminescence properties of the ⁴T₂ and ²E energy levels in Cr³⁺ are completely different since the emission spectrum of Cr3+ in the six-coordinated sites is determined by the crystal field strength that is sensitive to the local coordination environment. 19 Cr3+ can produce broadband NIR emission in the range of 650-1350 nm when located in a weak octahedral coordination crystal field making it the first choice for broadband NIR luminescence activators. 2,20-22 Lanthanide (Ln) group metal cations have been found to boost the photovoltaic performance of perovskite solar cells by passivating uncoordinated halide ions and improving the stability.23-25 In particular, Yb3+ ions can emit at around 900-1000 nm and are considered as ideal spectral converters. Inspired by the possible energy transfer between Cr3+ and Yb3+ ions, as well as the close effective ionic radius of Yb3+ (0.87 Å when CN = 6) to In^{3+} (0.80 Å when CN = 6), Cr^{3+} and Yb^{3+} codoped phosphors were developed to further improve their application potential.²⁶ Therefore, introducing Cr³⁺ and Yb³⁺ into Cs₂AgInCl₆ is a promising approach to develop new NIR emitting phosphors with the characteristics of broad emission and a high PLQY.

In this work, we have synthesized an efficient Cr³⁺ and Yb³⁺ co-doped CAIC DPSC NIR-emitting phosphor by a facile hydrothermal method. The crystal structures of CAIC, CAIC:Cr³⁺ and CAIC:Cr³⁺,Yb³⁺ DPSCs were determined by X-ray diffraction (XRD) while the morphology was characterized by scanning electron microscopy (SEM). X-ray photoelectron spectroscopy

(XPS) was conducted to further characterize the electronic and crystal structures. Optical studies revealed that CAIC:Cr $^{3+}$,Yb $^{3+}$ DPSCs show broadband NIR emission ($\lambda_{max}=1000$ nm, FWHM = 188 nm) and a high PLQY (\sim 45%) with 365 nm excitation. The enhancement mechanism has also been discussed. Furthermore, we combined the DPSCs with a 365 nm LED chip to prepare a pc-LED and demonstrated applications in vein imaging and night vision.

2. Results and discussion

The structures of the CAIC:Cr³⁺ DPSCs were determined using SHELXT and OLEX2. The corresponding crystallographic parameters are given in Tables S1-S4 in the ESI.† The CAIC:Cr3+ DPSCs were found to have the traditional perovskite structure with the $Fm\bar{3}m$ space group where the $[AgCl_6]^{5-}$ and $[InCl_6]^{3-}$ [CrCl₆]³⁻ octahedra shared the halide atoms at the corner to form a 3D structure. By introducing Cr³⁺ into the pristine Cs₂AgInCl₆ perovskite single crystal structure, the lattice parameter and cell volume were reduced from the original magnitude due to the relatively smaller ionic radius of Cr3+, validating that Cr3+ ions successfully entered the lattice to partially replace In³⁺ ions.²⁷ Fig. S1[†] shows the SEM images of CAIC, CAIC:30%Cr³⁺ and CAIC:30%Cr³⁺,3%Yb³⁺ DPSCs, respectively. As seen from the SEM images, all of them have an octahedral shape with average sizes of 500 µm. X-ray diffraction (XRD) of CAIC:Cr3+ and CAIC:Cr3+,Yb3+ DPSCs was also measured, and the results are shown in Fig. 1b. The cubic phase was observed for all the DPSC samples, with no noticeable impurity being detected. The introduction of Cr3+ and Yb3+ has no effect on the structure of CAIC. Compared with the XRD results of CAIC: Cr3+, the intensity of the diffraction peaks for the 220 crystal plane increases significantly after introducing Yb3+, indicating greatly improved crystallinity of the DPSCs. Notably, the XRD diffraction peaks for the (220) crystal plane were shifted monotonically to a larger angle with the increase of the Cr3+ concentration due to substituting smaller Cr3+ ions for the larger In3+ ions. The XRD patterns of the samples with different amounts

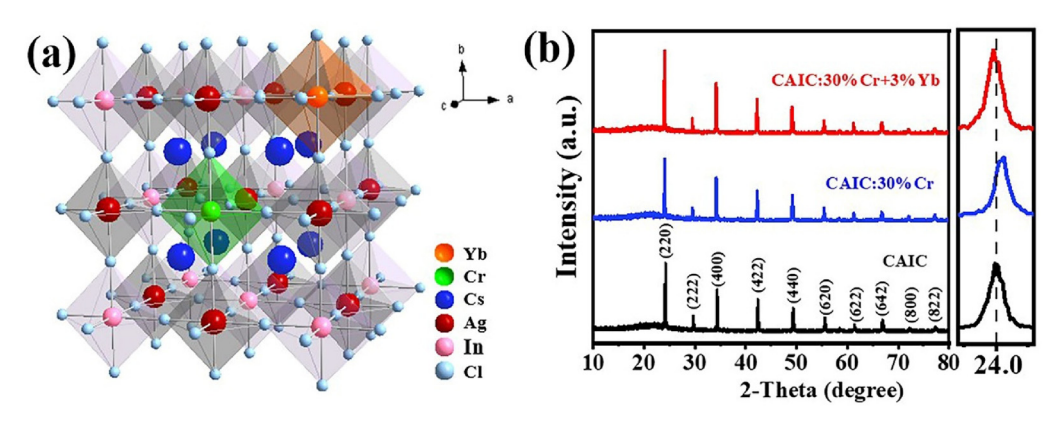


Fig. 1 (a) Schematic illustration of the crystal structure of Cr^{3+} , Yb^{3+} doped CAIC DPSCs. (b) XRD patterns of Cr^{3+} , Yb^{3+} doped CAIC DPSCs and (220) local enlarged view of the crystal plane.

of Cr³⁺ and Yb³⁺ are shown in Fig. S2 and S3.† The diffraction peak of the (220) crystal plane of CAIC:Cr3+,Yb3+ shifted to a smaller angle compared to that of CAIC:Cr3+ due to the larger ionic radius of Yb³⁺ than that of In³⁺ causing lattice expansion.

EDS spectra were measured to determine the elemental composition of CAIC:30%Cr3+. Fig. S4(a-f)† show the EDS images of CAIC:Cr3+ DPSCs. Elements of Cs, In, Ag, Cl and Cr are found in the EDS spectrum and evenly distributed in the whole DPSCs. The actual doping content of Cr³⁺ and Yb³⁺ was determined using ICP-OES and ICP-MS, with the results given in Table S5,† which is lower than the initial content introduced in the synthesis. In the following, we use the feed molar ratio for discussion.

The elemental composition and electronic properties of CAIC:Cr³⁺,Yb³⁺ were further characterized using XPS, and the results confirm the existence of all the elements in CAIC:Cr³⁺, Yb³⁺ (Fig. 2a-f). In the high-resolution Cr 2p spectrum (Fig. 2e), the peaks of 587.1 and 576.9 eV can be assigned to Cr $2p_{1/2}$ and Cr $2p_{3/2}$, and no peaks associated with Cr⁴⁺ were found, supporting that Cr remains in the +3 valence state. 28 A peak at 572.4 eV is assigned to Ag 3p_{3/2}. The binding energy of Cr 2p is consistent with the binding energy of octahedral Cr³⁺ ions reported in earlier studies.^{21,29} In addition, the peaks of In 3d and Cl 2p all shifted toward a lower binding energy due to Yb³⁺ incorporation, which is attributed to the smaller electronegativity of Yb than that of In, leading to stronger Yb-Cl bonding.30

The diffuse reflectance spectra (DRS) of the samples are shown in Fig. 3a. CAIC:Cr³⁺ shows three broad absorption bands with maxima at around 365 nm, 550 nm and 830 nm. The main 365 nm band is attributed to the electronic transition from the valence band to the conduction band of the CAIC host. After calculating and extrapolating using a linear function to the photon energy axis, the bandgap of pristine CAIC was estimated to be about 3.2 eV, as shown in the inset of Fig. 3a, which is consistent with a previous report.³¹ The absorption bands at 550 nm and 830 nm can be ascribed to Cr^{3+} d-d transitions of ${}^{4}A_{2} \to {}^{4}T_{1}$ and ${}^{4}A_{2} \to {}^{4}T_{2}$. The DRS spectrum of CAIC:Cr3+ and CAIC:Cr3+,Yb3+ shows similar absorption positions. Fig. S5† shows the PL excitation spectra (PLE) of CAIC:Cr³⁺ and CAIC:Cr³⁺,Yb³⁺ with an emission wavelength of 1000 nm being monitored. The PLE spectra agree with the DRS spectrum. Besides, the PLE spectra of the Yb-doped sample exhibit identical spectral shapes, indicating that the emission originates from the same transition. The three PLE bands at 365, 550, and 830 nm can be assigned as in the DRS.

The PL spectra of CAIC:Cr³⁺,Yb³⁺ DPSCs with 365 nm excitation are shown in Fig. 3b. CAIC:30%Cr3+ DPSCs have a broadband emission in the range of 800 to 1400 nm with the maxima at 1000 nm and FWHM = 180 nm, which is ascribed to the ${}^4\mathrm{T_2}{}^-{}^4\mathrm{A_2}$ transition of Cr^{3+} . The addition of Yb^{3+} did not change the position of the emission band but increased its intensity and FWHM to 188 nm. This broad emission bands covered the NIR-I (700-900 nm) and NIR-II (1000-1700 nm) biowindows, which are broader than those of many recently reported NIR phosphors, such as LaMgGa₁₁O₁₉:Cr³⁺ (138 nm)³² and MgTa₂O₆:Cr³⁺ (140 nm).³³ The increased PL intensity indicated suppressed non-radiative recombination by Yb3+ doped CAIC:Cr³⁺. The PLQY of the best sample is about 45% (Fig. S6†) which is much higher than those of Cs2NaInCl6:Cr3+ (PLQY = 19.7%) and $Cs_2AgInCl_6:Yb^{3+}$ (PLQY = 0.2%). The PL spectra of Yb-doping CAIC:Cr3+ with different Yb3+ concentrations, as shown in Fig. S7,† exhibited a blue-shift for CAIC:Cr3+,Yb3+ DPSCs compared with the CAIC:Cr3+ DPSCs, which is attributed

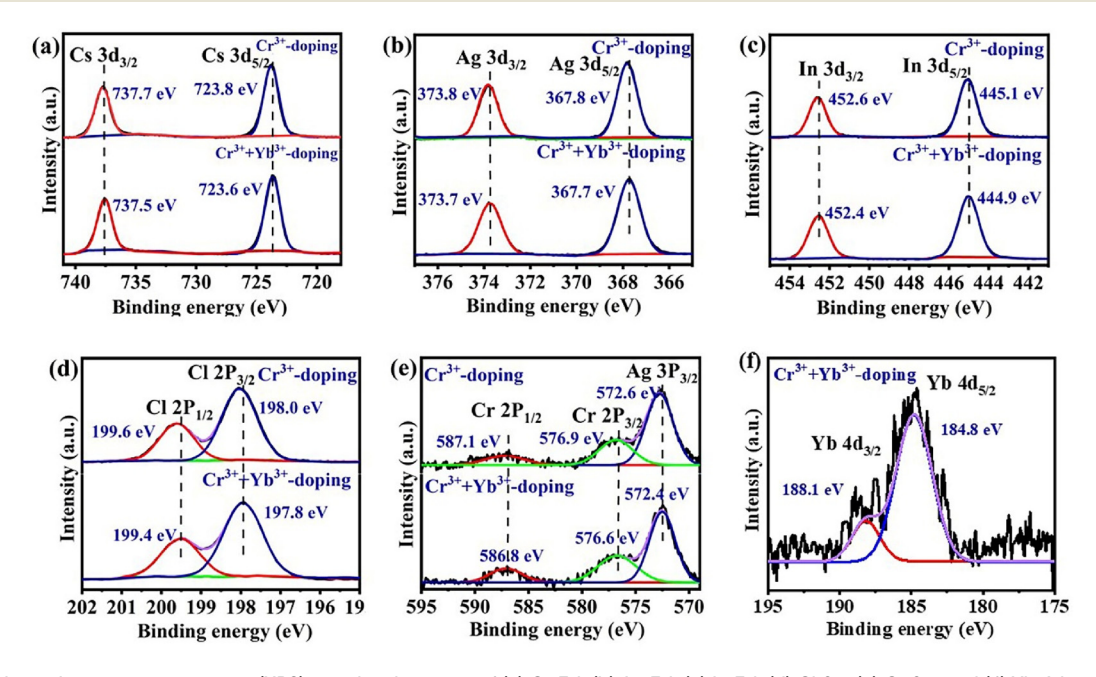


Fig. 2 X-ray photoelectron spectroscopy (XPS) core level spectra of (a) Cs 3d, (b) Ag 3d, (c) In 3d, (d) Cl 2p, (e) Cr 2p, and (f) Yb 4d.

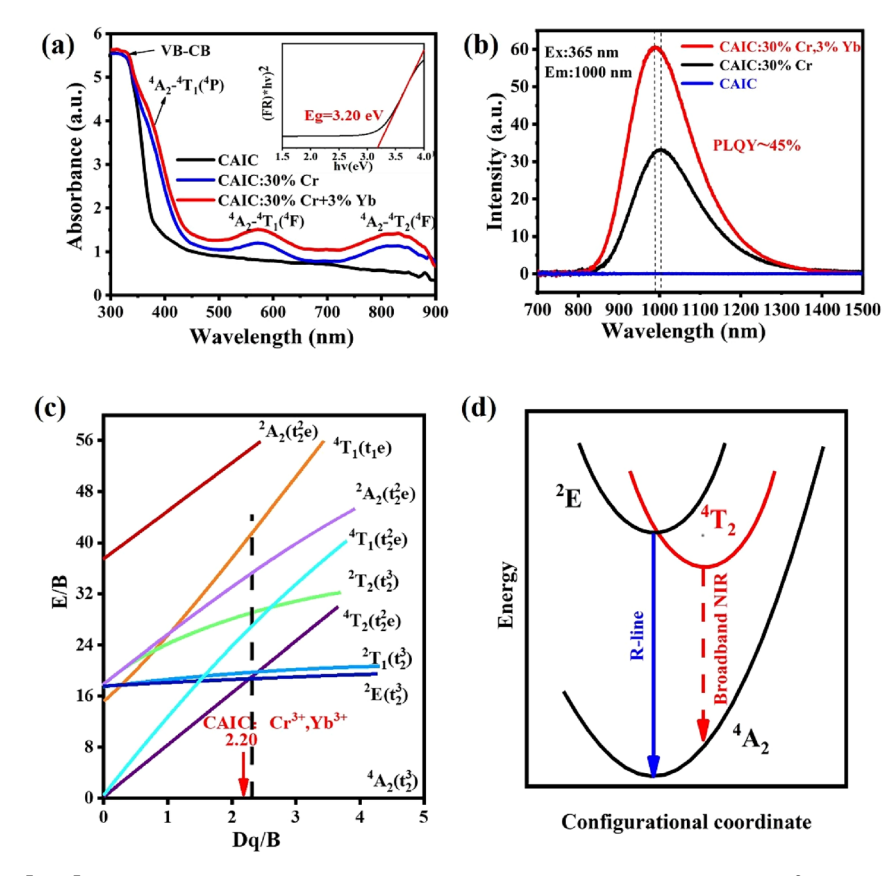


Fig. 3 (a) DRS of CAIC: Cr^{3+} , Yb^{3+} . The inset shows the DR spectrum of the CAIC DPSC host with $[F(R) \times hv]^2$ as a function of photon energy, for determining the band gap energy. (b) PL spectra of CAIC: Cr^{3+} , Yb^{3+} DPSCs. (c) Tanabe–Sugano energy level diagram of Cr^{3+} in an octahedral crystal field. (d) Configurational coordinate diagram of Cr^{3+} in a weak crystal field.

to the passivation of shallow trap states in CAIC: ${\rm Cr}^{3^+}$, ${\rm Yb}^{3^+}$ DPSCs as discussed in more detail later.

The PL spectra with different excitation wavelengths shown in Fig. S8† vary in intensity but maintain the same shape with the excitation wavelength changing from 320 to 600 nm, indicating that the NIR emission originates from the same transition. In addition, we used the same method to synthesize CAIC:Yb³+, with its PL spectrum shown in Fig. S9.† The emission band of CAIC:Yb³+ has the same position as that of CAIC: Cr³+, but has a different emission origin. The emission of CAIC:Cr³+ can be ascribed to Cr³+ d–d transitions and the emission of CAIC:Yb³+ can be attributed to the $^2F_{5/2} \rightarrow ^2F_{7/2}$ transition of Yb³+ f electrons and thus exhibits a narrower FWHM and lower PLQY. 16

Upon introducing Cr^{3+} to $Cs_2AgInCl_6$, the Cr^{3+} ions (r=0.62 Å, CN=6) were proposed to substitute In^{3+} ions (r=0.8 Å, CN=6) due to their similar ionic radius and same oxidation state, forming the $[CrCl_6]^{3-}$ octahedron. Because of the symmetry decrease of the potential octahedron field, the 3d orbital of the Cr^{3+} ion degraded to the double degenerated $d_{x^2-y^2}$ and d_{z^2} (eg) states and the triple degenerated d_{xy} , d_{xz} , and d_{yz} (t2g) states. This process can be explained by the Tanabe–Sagano diagram (Fig. 3c). The emission of Cr^{3+} ions is strongly dependent on the crystal field environment of the lattice. In the case of a strong crystal field, the transition from

the 2 E to 4 A $_2$ energy level is spin-forbidden, resulting in narrowband red light from the 2 E energy level (marked as an R-line in Fig. 3d). In a weak crystal field, the 4 T $_2$ energy level transitions to the ground state are allowed, resulting in broadband NIR light from the 4 T $_2$ energy level. According to energy level splitting, the crystal field strength is defined by relative positions of the 4 T $_2$ and 2 E energy levels. The following equations can be used to obtain Dq/B:

$$Dq = E(^{4}A_{2} \to {}^{4}T_{2})/10 \tag{1}$$

$$\frac{\mathrm{Dq}}{B} = \frac{15\left(\frac{\Delta E}{\mathrm{Dq}} - 8\right)}{\left(\Delta E/\mathrm{Dq}\right)^2 - 10(\Delta E/\mathrm{Dq})} \tag{2}$$

where $E(^4A_2 \rightarrow {}^4T_2)$ is the energy difference between 4T_2 and 4A_2 energy levels (in cm⁻¹) and ΔE is the energy difference between $E(^4A_2 \rightarrow {}^4T_1)$ and $E(^4A_2 \rightarrow {}^4T_2)$ transitions. Dq is called the crystal field splitting parameter, and B is the Racah parameter. Using the data in Fig. 3a, the values of Dq/B are 2.20 and 2.25 (Fig. 3c) in CAIC:Cr³⁺,Yb³⁺ DPSCs and in CAIC:Cr³⁺, respectively. When the Dq/B value was larger than 2.3, Cr³⁺ ions were in a strong crystal field. When the Dq/B value was smaller than 2.3, Cr³⁺ ions were in a weak crystal field. This indicates that the Cr³⁺ ions are in a weak crystal field in the CAIC:Cr³⁺,Yb³⁺ host. As shown in Fig. 3c, the energy separ-

ation between energy levels 4T_2 and 4A_2 is narrow. Therefore, CAIC:Cr $^{3+}$,Yb $^{3+}$ exhibits broadband NIR emission (800 to 1400 nm), and the emission band is centered at a much longer wavelength (1000 nm) than those of other Cr $^{3+}$ -doped NIR phosphors such as BaMgAl $_{10}$ O $_{17}$:Cr $^{3+}$ (762 nm) 42 and LiScP $_2$ O $_7$:0.06Cr $^{3+}$ (880 nm). 43

To gain deeper insight into the PL mechanism of the Yb³⁺-doped CAIC:Cr³⁺ DPSCs, we measured the time-resolved PL (TRPL) decay profiles, as shown in Fig. 4a. The TRPL of CAIC: ${\rm Cr}^{3+}, {\rm Yb}^{3+}$ was collected with excitation at 365 nm and emission monitored at 1000 nm. All of the decay curves were fit by a single exponential function, with the time being constant at the microsecond time scale, which was consistent with a previous report.²² This also indicated that the emission was mainly from the transition of ${}^4{\rm T}_2$ to ${}^4{\rm A}_2$ of ${\rm Cr}^{3+}$. We can use eqn (3) and (4) to calculate radiative $(\tau_{\rm r})$ and non-radiative $(\tau_{\rm nr})$ components of the observed PL lifetime $(\tau_{\rm obs})$.

$$PLQY = \frac{\tau_{obs}}{\tau_{r}}$$
 (3)

$$\frac{1}{\tau_{\rm obs}} = \frac{1}{\tau_{\rm r}} + \frac{1}{\tau_{\rm nr}} \tag{4}$$

The calculated values for τ_r and τ_{nr} are summarized in Table 1. Both radiative and non-radiative lifetimes increase significantly with Yb³+ doping. This indicates that Yb³+ doping affects both the radiative and non-radiative pathways. The effect on radiative pathways suggests electronic interaction between Cr³+ and Yb³+ ions. The longer non-radiative lifetime may be attributed to the lower density of trap states upon Yb³+ co-doping that has some passivation effect on defects. 44

Ln³⁺ doping has been suggested to passivate anion defects due to strong Ln–X bonding that reduces the formation of defects and increases the exciton lifetime of perovskites. 36,45 The PL spectra and TRPL profiles of CAIC:Cr³⁺,Er³⁺ and CAIC: Cr³⁺,Ho³⁺ DPSCs were measured and are shown in Fig. S10 and S11.† Doping Ho³⁺ or Er³⁺ to CAIC:Cr³⁺ DPSCs also leads to an enhanced PL intensity and longer observed PL lifetime (15.30 μs and 20.48 μs). Compared to Ho³⁺ and Er³⁺, Yb³⁺ with a relatively smaller electronegativity and ionic radius has a stronger effect on the PL properties. The smaller electronegativity and ionic radius Yb³⁺ are expected to lead to stronger Yb–Cl bonding, 30 which is supported by XPS results. The

Table 1 Calculated radiative and nonradiative lifetimes for CAIC:30% ${\rm Cr}^{3+}$ and CAIC:30% ${\rm Cr}^{3+},3\%{\rm Yb}^{3+}$

Sample	$ au_{\mathrm{obs}}\left(\mu s\right)$	$\tau_{\mathrm{r}} (\mu \mathrm{s})$	$\tau_{\mathrm{nr}}\left(\mu s\right)$	PLQY
CAIC:30%Cr ³⁺	10.81	48.0	14.0	22.5%
CAIC:30%Cr ³⁺ ,3%Yb ³⁺	32.03	71.1	58.5	45%

strong interaction between Yb3+ and Cl- can improve the crystallinity and reduce the surface energy of crystal growth; Cl⁻ anions would firstly interact with Yb3+ which would lead the Yb³⁺ absorbed on the colloidal cluster to form large grains to improve the crystallinity and reduce the formation of defects. 23,46 The origin for PL enhancement in CAIC:Cr3+,Yb3+ DPSCs is attributed to structural modification upon Yb³⁺ doping, as shown in Fig. 4b. The pristine perovskite structure possesses more Cl vacancies (VCl) and InAg vacancies (represented by black spheres).⁴⁷ The ionic radius of the Yb³⁺ ion is closer to that of the In3+ ion than that of Cr3+; thus the addition of the Yb³⁺ ion alleviates the distorted [InCl₆]³⁻ octahedra caused by the addition of the Cr3+ ion and the introduction of Yb3+ can reduce the surface energy to influence the growth of crystals. As a result, the PL intensity of the NIR-II emission was enhanced by doping with Yb3+.

To determine the role of Yb³⁺ incorporation in boosting the Cr³⁺ emission, we measured the PL spectra of CAIC, CAIC:Cr³⁺, CAIC:Yb3+, and CAIC:Cr3+,Yb3+ samples in the 450-800 nm region, as shown in Fig. S12a,† in which the host emission intensity was improved with Yb³⁺ doping. Fig. S12b† shows the spectral overlap between the PLE band of CAIC:Cr3+ monitored at 1000 nm and the PL spectrum of CAIC:Yb3+ excited at 365 nm. We suggest that there is energy transfer (ET) from the STEs to Cr³⁺ in the co-doped CAIC. Moreover, the incorporation of the Yb3+ ions can induce an elongation of the bond lengths of the [CrCl₆]³⁻ octahedra associated, and thus a decrease of the energy gap between the ${}^{2}E(g)$ and ${}^{4}T_{2}(g)$ states of Cr³⁺, which triggers the occurrence of the structural confinement effect and promoted the ET of STEs to Cr³⁺. 48,49 Overall, as shown in Fig. S13,† we attribute the enhancement of PL to the synergistic effect of reduced non-radiative recombination due to defect passivation and energy transfer from STEs to Cr3+.

To further understand the effect of Yb³⁺ ion doping on the thermal stability of the samples, the PL spectra of CAIC:Cr³⁺

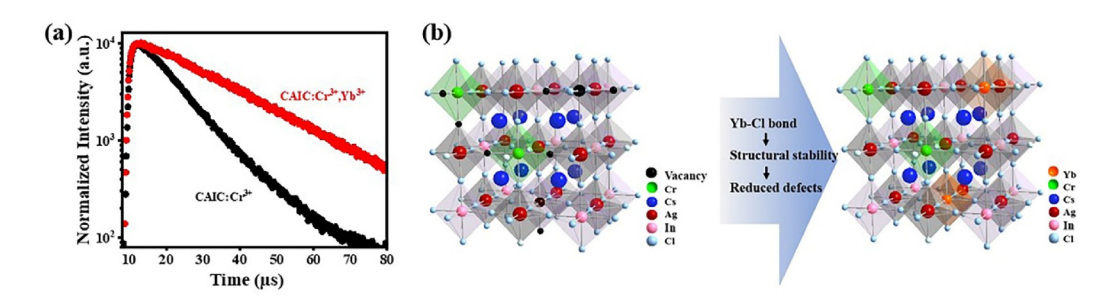


Fig. 4 (a) Time-resolved PL decay profiles of CAIC: Cr^{3+} , and CAIC: Cr^{3+} , Yb³⁺. (b) Schematic illustration of the structure of CAIC: Cr^{3+} DPSCs with defects and CAIC: Cr^{3+} , Yb³⁺ with structural modification.

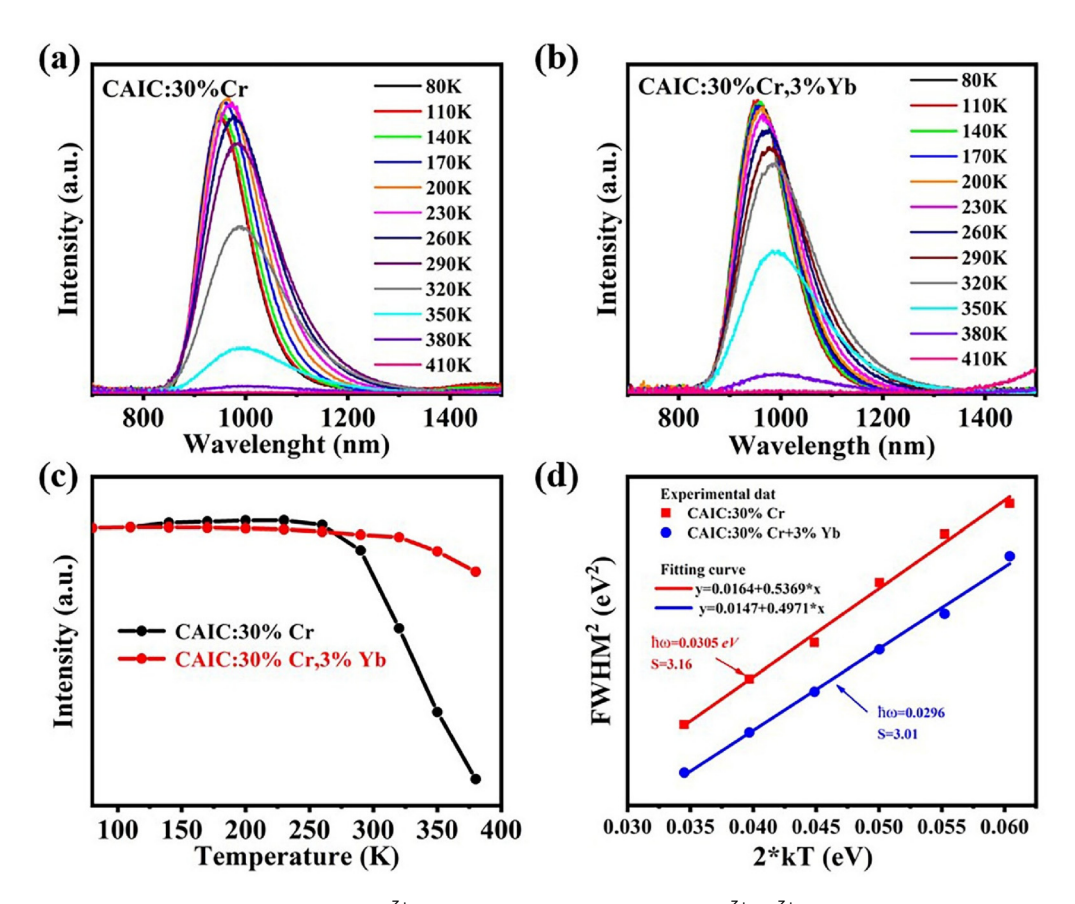


Fig. 5 Temperature-dependent PL spectra of (a) CAIC:Cr³⁺ excited at 365 nm and (b) CAIC:Cr³⁺,Yb³⁺ excited at 365 nm. (c) The dependence of the PL intensity of CAIC: Cr^{3+} and CAIC: Cr^{3+} , Yb^{3+} on temperature. (d) The fitting results of FWHM² as a function of 2kT.

and CAIC:Cr3+,Yb3+ DPSCs at different temperatures were measured, as shown in Fig. 5a and b. Fig. S13† illustrates the photophysical process in Cr³⁺-incorporated CAIC DPSCs. With photoexcitation at 365 nm, the electrons are excited from the valence band (VB) to the conduction band (CB) of the CAIC DPSC host. The energy from the host can be transferred to the ⁴T₂ state of Cr³⁺ ions which then results in the ⁴T₂-⁴A₂ transition. The energy of the host can also be transferred to the self-trapped exciton (STE) state, resulting in a broad emission (process 1),⁵⁴ or to the Cr³⁺ ion (process 2) that leads to the ⁴T₂-⁴A₂ transition. Fig. S14† shows the PL spectra in the visible region of the CAIC:30%Cr³⁺ sample at 80 K and 200 K, which originates from process 1 as shown in Fig. S13.† The emission of STEs was observed at low temperature and quenched at above 200 K. From 80 K to 200 K, the PL in the visible region decreased with increasing temperature due to the electron-phonon coupling thermal; at the same time, the NIR emission increased due to much energy transfer from the STEs to Cr3+, which is similar to previous reports.50-53 With further increase in the temperature, the emission was decreased, attributed to the increase of non-radiative transition processes mediated by phonons. At 350 K, CAIC:Cr³⁺ and CAIC: Cr^{3+} , Yb^{3+} DPSCs retained 15.47% and 49.61% of their original intensities at 80 K, indicating that the thermal stability of the material was improved with the addition of Yb³⁺ (Fig. 5c). This may be related to the difference in the electron-phonon coupling between CAIC:Cr³⁺ and CAIC:Cr³⁺,Yb³⁺. Generally, we can use eqn (5) to calculate the coupling effect between electrons and phonons by fitting the FWHM of the PL spectrum with temperatures.⁵⁵

$$FWHM = 2.36\sqrt{S}\hbar\omega\sqrt{\coth\left(\frac{\hbar\omega}{2kT}\right)}$$
 (5)

where $\hbar\omega$ stands for the phonon frequency, T is the Kelvin temperature, S means the Huang-Rhys parameter and kmeans the Boltzmann constant. When regrading $\frac{\hbar \omega}{2kT}$ as x, coth(x) is equivalent to $\frac{e^x + e^{-x}}{e^x - e^{-x}}$. Owing to $\frac{\hbar\omega}{2kT} = 10^{-3}$, eqn (5) can be simplified as eqn (6).

$$FWHM^{2} = 5.57 \times S \times (\hbar\omega)^{2} \left(1 + \frac{1}{\frac{\hbar\omega}{2kT}}\right)$$
 (6)

Eqn (6) can be written as:

$$FWHM^2 = A \times 2kT + B \tag{7}$$

where $A = 5.57 \times S \times \hbar\omega$ and $B = 5.57 \times S \times (\hbar\omega)^2$. The fitting results are shown in Fig. 5d. The $\hbar\omega$ and S for CAIC:Cr³⁺ are 0.0305 eV and 3.16, and those for CAIC:Cr³⁺,Yb³⁺ are 0.0296 eV and 3.01, revealing a strong electron-phonon coupling effect in CAIC:30%Cr³⁺. A smaller S value suggests that the electronphonon coupling effect in CAIC:Cr³⁺,Yb³⁺ is weaker than that in CAIC:Cr³⁺. Therefore, the thermal stability of CAIC:Cr³⁺,Yb³⁺ is stronger than that of CAIC:Cr³⁺. Furthermore, we calculated the exciton binding energy of CAIC:30%Cr3+ and CAIC:30% Cr³⁺,3%Yb³⁺ using temperature-dependent PL spectra (Fig. 5a and b), from which the corresponding exciton binding energy (E_b) is derived as 215 meV and 242 meV (Fig. S15†) according to eqn (8).

$$I(T) = \frac{I_0}{1 + Ae^{\left(-\frac{E_b}{kT}\right)}} \tag{8}$$

Combined with the calculated optical phonon energy analysis, we suggest that the CAIC:30%Cr³⁺,3%Yb³⁺ DPSC samples have a higher exciton binding energy and relatively lower phonon disturbance, indicating suppressed non-radiative relaxation. 42,56 Therefore, doping Yb3+ could effectively suppress the strong exciton-phonon interaction and improve the radiative transition probability and PLQY. This facilitates the application of crystals for near-infrared light emission and light-emitting devices. In addition, the NIR emission band center position shifted from 964 to 1000 nm as the temperature increased from 80 to 380 K, which can be explained by the change in the crystal field strength. As the temperature increased, the lattice vibration increased and the lattice expanded, which ultimately weakened the crystal field. According to the Tanabe-Sugano energy level diagram of Cr3+ (Fig. 3c), a weakening of the crystal field will result in a redshift of the emission spectrum.⁵⁷

As a demonstration of potential applications, the CAIC: ${\rm Cr}^{3+}$,Yb $^{3+}$ DPSCs were applied with the InGaN chip ($\lambda_{\rm em}$ = 365 nm) to prepare NIR pc-LED samples. Fig. 6a shows the driving current dependent electroluminescence (EL) spectra of the pc-LED device. The NIR EL intensity increased with increasing current. Besides, Fig. 6b shows a NIR output of 18.0 mW@190 mA, and the conversion efficiency reached 9.45% @10 mA. We used the prepared pc-LED to test muscle

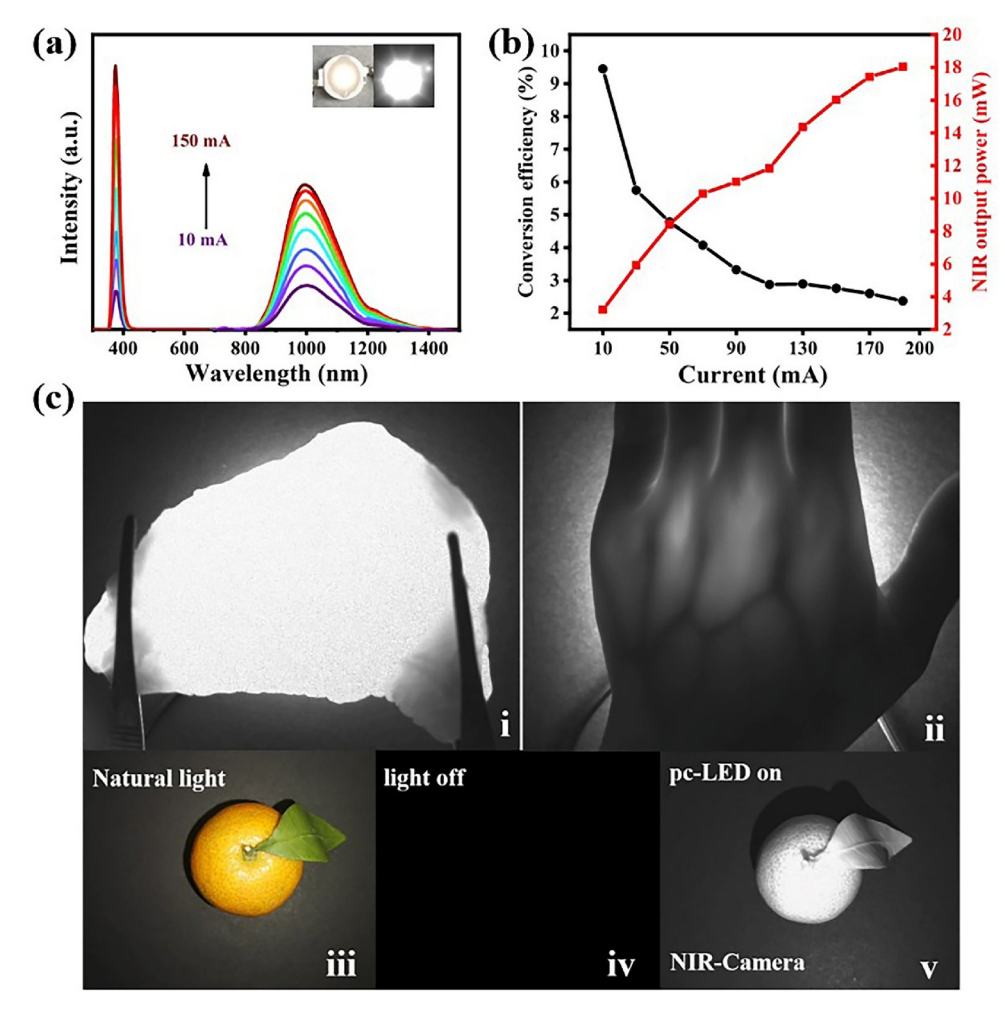


Fig. 6 (a) Driven current dependent emission spectra of the fabricated NIR pc-LED. (b) Conversion photoelectric efficiency and NIR output power of the pc-LED. (c) Photograph of the transmission photographs of a 2.5 cm chicken breast (i) and the veins in the palm (ii) taken with a NIR camera. (iii-v) A photo of an orange taken with natural light on (iii) and off (iv) captured with a visible camera and NIR pc-LED light using a NIR camera (v).

tissue transmission, human vein imaging, and night vision ability, as shown in Fig. 6c. The results showed that the intensity of NIR radiation is sufficient to penetrate a 2.5 cm chicken breast (Fig. 6ci), and the vein distribution of the palm can be clearly observed (Fig. 6cii). In addition, a photo of an orange was taken with a visible light camera under light (Fig. 6ciii) and in the dark (Fig. 6civ). When the NIR-LED was turned on, the orange could be observed using the NIR camera (Fig. 6cv). These results suggest that CAIC:Cr³⁺,Yb³⁺ is promising for human vein imaging and night vision.

3. Conclusion

In conclusion, we synthesized broadband NIR co-doped CAIC: Cr3+,Yb3+ DPSCs by a facile hydrothermal method. Under 365 nm excitation, the as-prepared co-doped CAIC:Cr³⁺,Yb³⁺ DPSCs show a broadband NIR emission at 1000 nm with a fullwidth at half maximum (FWHM) of 188 nm and a PLQY of ~45%. The enhanced PLQY is attributed to the synergistic effect of reduced non-radiative recombination due to defect passivation and increase in crystallinity, and energy transfer (ET) of STEs to Cr³⁺. With the aid of a NIR camera, a pc-LED was fabricated and used as a light source to capture clear images of veins in the palm. Furthermore, the feasibility of a pc-LED for night vision applications was successfully demonstrated. This study suggests that the synthesized CAIC:Cr³⁺, Yb³⁺ DPSCs are promising for biomedical imaging applications.

Conflicts of interest

The authors declare no competing financial interest.

Acknowledgements

This work was supported by the National Natural Science Foundation of China (Grant No. 21965003) and the Opening Project of Guangxi Key Laboratory of Marine Natural Products and Combinatorial Biosynthesis Chemistry (Grant No. GXMNPC2020003). JZZ acknowledges the US NSF (CHE-1904547) for financial support.

References

- 1 M. Mao, T. Zhou, H. Zeng, L. Wang, F. Huang, X. Tang and R.-J. Xie, Broadband Near-infrared (NIR) Emission Realized by the Crystal-field Engineering of $Y_{3-x}Ca_xAl_{5-x}SixO_{12}$: $Cr^{3+}(x=0-2.0)$ Garnet Phosphors, *J. Mater. Chem. C*, 2020, **8**, 1981–1988.
- 2 D. Dai, Z. Wang, Z. Xing, X. Li, C. Liu, L. Zhang, Z. Yang and P. Li, Broad Band Emission Near-infrared Material Mg₃Ga₂GeO₈:Cr³⁺: Substitution of Ga-In, Structural

- Modification, Luminescence Property and Application for High Efficiency LED, *J. Alloys Compd.*, 2019, **806**, 926–938.
- 3 T. Appadurai, S. Chaure, M. Mala and A. K. Chandiran, Role of Copper in Enhancing Visible Light Absorption in Cs₂Ag(Bi, In, Sb)Cl₆ Halide Double-Perovskite Materials, *Energy Fuels*, 2021, 35, 11479–11487.
- 4 R. Marin and D. Jaque, Doping Lanthanide Ions in Colloidal Semiconductor Nanocrystals for Brighter Photoluminescence, *Chem. Rev.*, 2021, **121**, 1425–1462.
- 5 I. Infante and L. Manna, Are There Good Alternatives to Lead Halide Perovskite Nanocrystals, *Nano Lett.*, 2021, 21, 6-9.
- 6 H. Arfin, A. S. Kshirsagar, J. Kaur, B. Mondal, Z. Xia, S. Chakraborty and A. Nag, ns² Electron (Bi³⁺ and Sb³⁺) Doping in Lead-Free Metal Halide Perovskite Derivatives, *Chem. Mater.*, 2020, 32, 10255–10267.
- 7 F. Igbari, Z.-K. Wang and L.-S. Liao, Progress of Lead–Free Halide Double Perovskites, *Adv. Energy Mater.*, 2019, **9**, 1803150.
- 8 K. Dave, M. H. Fang, Z. Bao, H. T. Fu and R. S. Liu, Recent Developments in Lead-Free Double Perovskites: Structure, Doping, and Applications, *Chem. Asian J.*, 2020, **15**, 242–252.
- 9 R. Sun, D. Zhou and H. Song, Rare Earth Doping in Perovskite Luminescent Nanocrystals and Photoelectric Devices, *Nano Select*, 2021, 3, 531–554.
- 10 J. Zhou, X. Yun, R. Wang, D. Xu and X. Li, Self-trapped Exciton to Dopant Energy Transfer in Sb³⁺-doped Cs₂ZrCl₆ Perovskite Variants, *Mater. Chem. Front.*, 2021, 5, 6133.
- 11 Y. Yao, S.-W. Zhang, Z. Liu, C.-Y. Wang, P. Liu, L. Ma, G. Wei and F. Kang, Air Stable and Highly Efficient Bi³⁺-doped Cs₂SnCl₆ for Blue Light-emitting Diodes, *RSC Adv.*, 2021, **11**, 26415–26420.
- 12 Z. Xu, W. Liu, Z. Wang and L. Hanzo, Petahertz Communication: Harmonizing Optical Spectra for Wireless Communications, *Digital Commun. Networks*, 2021, 7, 605–614
- 13 Y. Tang, S. Tang, M. Luo, Y. Guo, Y. Zheng, Y. Lou and Y. Zhao, All-inorganic Lead-Free Metal Halide Perovskite Quantum Dots: Progress and Prospects, *Chem. Commun.*, 2021, 57, 7465–7479.
- 14 J. Zhou, X. Rong, M. S. Molokeev, Y. Wang, X. Yun, D. Xu and X. Li, Alloying Cs⁺ into Rb₂ZrCl₆:Te⁴⁺ Toward Highly Efficient and Stable Perovskite Variants, *Mater. Chem. Front.*, 2021, 5, 4997–5003.
- 15 Y. Liu, A. Nag, L. Manna and Z. Xia, Lead-Free Double Perovskite Cs₂AgInCl₆, *Angew. Chem., Int. Ed.*, 2021, 60, 11592–11603.
- 16 Y. Mahor, W. J. Mir and A. Nag, Synthesis and Near-Infrared Emission of Yb-Doped Cs₂AgInCl₆ Double Perovskite Microcrystals and Nanocrystals, *J. Phys. Chem. C*, 2019, 123, 15787–15793.
- 17 H. Arfin, J. Kaur, T. Sheikh, S. Chakraborty and A. Nag, Bi $\binom{3^+}{}$ -Er $\binom{3^+}{}$ and Bi $\binom{3^+}{}$ -Yb $\binom{3^+}{}$ Codoped Cs₂AgInCl₆ Double Perovskite Near-Infrared Emitters, *Angew. Chem., Int. Ed.*, 2020, **59**, 11307–11311.

- 18 Q. Zhang, G. Li, P. Dang, D. Liu, D. Huang, H. Lian and J. Lin, Enhancing and Tuning Broadband Near-infrared (NIR) Photoluminescence Properties in Cr³⁺-doped Ca₂YHf₂Al₃O₁₂ Garnet Phosphors via Ce³⁺/Yb³⁺-codoping for LED Applications, *J. Mater. Chem. C*, 2021, 9, 4815– 4824.
- 19 D. Hou, H. Lin, Y. Zhang, J.-Y. Li, H. Li, J. Dong, Z. Lin and R. Huang, A broadband near-infrared phosphor BaZrGe₃O₉:Cr³⁺: luminescence and application for light-emitting diodes, *Inorg. Chem. Front.*, 2021, **8**, 2333–2340.
- 20 Z. Wu, X. Han, Y. Zhou, K. Xing, S. Cao, L. Chen, R. Zeng, J. Zhao and B. Zou, Efficient Broadband Near-infrared Luminescence of Cr³⁺ Doped Fluoride K₂NaInF₆ and Its NIR-LED Application toward Veins Imaging, *Chem. Eng. J.*, 2022, 427, 131740.
- 21 W. Zhou, J. Luo, J. Fan, H. Pan, S. Zeng, L. Zhou, Q. Pang and X. Zhang, Luminescent Properties and LED Application of Broadband Near-Infrared Emitting NaInGe₂O₆:Cr³⁺ phosphors, *Ceram. Int.*, 2021, 47, 25343–25349.
- 22 F. Zhao, Z. Song, J. Zhao and Q. Liu, Double perovskite Cs₂AgInCl₆:Cr³⁺: broadband and near-infrared luminescent materials, *Inorg. Chem. Front.*, 2019, **6**, 3621–3628.
- 23 K. Wang, L. Zheng, T. Zhu, X. Yao, C. Yi, X. Zhang, Y. Cao, L. Liu, W. Hu and X. Gong, Efficient Perovskite Solar Cells by Hybrid Perovskites Incorporated with Heterovalent Neodymium Cations, *Nano Energy*, 2019, 61, 352–360.
- 24 J. S. Yao, J. Ge, B. N. Han, K. H. Wang, H. B. Yao, H. L. Yu, J. H. Li, B. S. Zhu, J. Z. Song, C. Chen, Q. Zhang, H. B. Zeng, Y. Luo and S. H. Yu, Ce³⁺-Doping to Modulate Photoluminescence Kinetics for Efficient CsPbBr₃ Nanocrystals Based Light-Emitting Diodes, *J. Am. Chem. Soc.*, 2018, 140, 3626–3634.
- 25 L. Wang, H. Zhou, J. Hu, B. Huang, M. Sun, B. Dong, G. Zheng, Y. Huang, Y. Chen, L. Li, Z. Xu, N. Li, Z. Liu, Q. Chen, L.-D. Sun and C.-H. Yan, A Eu³⁺-Eu²⁺ Ion Redox Shuttle Imparts Operational Durability to Pb-I Perovskite Solar Cells, *Science*, 2019, 363, 265–270.
- 26 D. Huang, Q. Ouyang, H. Xiao, B. Wang, H. Lian, Q. Zeng and J. Lin, Cr,Yb-codoped Ca₂LaHf₂Al₃O₁₂ Garnet Phosphor: Electronic Structure, Broadband NIR Emission and Energy Transfer Properties, *Dalton Trans.*, 2021, 50, 908–916.
- 27 H. Yin, Y. Xian, Y. Zhang, W. Chen, X. Wen, N. U. Rahman, Y. Long, B. Jia, J. Fan and W. Li, An Emerging Lead–Free Double–Perovskite Cs₂AgFeCl₆:In Single Crystal, *Adv. Funct. Mater.*, 2020, 30, 2002225.
- 28 X. Duan, J. Liu, Y. Wu, F. Yu and X. Wang, Structure and Luminescent Properties of Co²⁺/Cr³⁺ Co-doped ZnGa₂O₄ Nanoparticles, *J. Lumin.*, 2014, **153**, 361–368.
- 29 A. M. Salvi, J. E. Castle, J. F. Watts and E. Desimoni, Peak Fitting of the Chromium 2p XPS Spectrum, *Appl. Surf. Sci.*, 1995, **90**, 333–341.
- 30 C. Lu, J. Zhang, D. Hou, X. Gan, H. Sun, Z. Zeng, R. Chen, H. Tian, Q. Xiong, Y. Zhang, Y. Li and Y. Zhu, Calcium Doped MAPbI₃ with Better Energy State Alignment in Perovskite Solar Cells, *Appl. Phys. Lett.*, 2018, 112, 193901.

- 31 J. Zhou, Z. Xia, M. S. Molokeev, X. Zhang, D. Peng and Q. Liu, Composition Design, Optical Gap and Stability Investigations of Lead-free Halide Double Perovskite Cs₂AgInCl₆, J. Mater. Chem. A, 2017, 5, 15031–15037.
- 32 S. Liu, Z. Wang, H. Cai, Z. Song and Q. Liu, Highly Efficient Near-infrared Phosphor LaMgGa₁₁O₁₉:Cr³⁺, *Inorg. Chem. Front.*, 2020, 7, 1467–1473.
- 33 G. Liu, M. S. Molokeev, B. Lei and Z. Xia, Two-site Cr³⁺ Occupation in the MgTa₂O₆:Cr³⁺ Phosphor toward Broadband Near-infrared Emission for Vessel Visualization, *J. Mater. Chem. C*, 2020, **8**, 9322–9328.
- 34 A. Zhang, Y. Liu, G. Liu and Z. Xia, Dopant and Compositional Modulation Triggered Broadband and Tunable Near-Infrared Emission in Cs₂Ag_{1-x}Na_xInCl₆:Cr³⁺ Nanocrystals, *Chem. Mater.*, 2022, **34**, 3006–3012.
- 35 J. Zhuang, P. Mao, Y. Luan, X. Yi, Z. Tu, Y. Zhang, Y. Yi, Y. Wei, N. Chen, T. Lin, F. Wang, C. Li and J. Wang, Interfacial Passivation for Perovskite Solar Cells: The Effects of the Functional Group in Phenethylammonium Iodide, ACS Energy Lett., 2019, 4, 2913–2921.
- 36 X. Zhuang, R. Sun, D. Zhou, S. Liu, Y. Wu, Z. Shi, Y. Zhang, B. Liu, C. Chen, D. Liu and H. Song, Synergistic Effects of Multifunctional Lanthanides Doped CsPbBrCl₂ Quantum Dots for Efficient and Stable MAPbI₃ Perovskite Solar Cells, Adv. Funct. Mater., 2022, 18, 2110346.
- 37 P. R. Varadwaj, A₂AgCrCl₆ (A = Li, Na, K, Rb, Cs) halide double perovskites: a transition metal-based semiconducting material series with appreciable optical characteristics, *Phys. Chem. Chem. Phys.*, 2020, 22, 24337–24350.
- 38 Z. Zou, X. Tang, C. Wu, D. Wang, J. Zhang, Z. Ci, S. Du and Y. Wang, How to tune trap properties of persistent phosphor: Photostimulated persistent luminescence of NaLuGeO₄:Bi³⁺,Cr³⁺ tailored by trap engineering, *Mater. Res. Bull.*, 2018, **97**, 251–259.
- 39 H. Xia, J. Wang, H. Wang, J. Zhang, Y. Zhang and T. Xu, Optical Spectroscopy and Crystal-field Strength of Cr³⁺ in Various Solid Matrixes, *Rare Met.*, 2006, 25, 51–57.
- 40 Y. Tanabe and S. Sugano, On the Absorption Spectra of Complex Ions II, *J. Phys. Soc. Jpn.*, 1954, **9**, 766–779.
- 41 H. Zeng, T. Zhou, L. Wang and R.-J. Xie, Two-Site Occupation for Exploring Ultra-Broadband Near-Infrared Phosphor-Double-Perovskite La₂MgZrO₆:Cr³⁺, *Chem. Mater.*, 2019, 31, 5245–5253.
- 42 L. You, R. Tian, T. Zhou and R.-J. Xie, Broadband Near-infrared Phosphor BaMgAl₁₀O₁₇:Cr³⁺ Realized by Crystallographic Site Engineering, *Chem. Eng. J.*, 2021, **417**, 129224.
- 43 L. Yao, Q. Shao, S. Han, C. Liang, J. He and J. Jiang, Enhancing Near-Infrared Photoluminescence Intensity and Spectral Properties in Yb³⁺ Codoped LiScP₂O₇:Cr³⁺, *Chem. Mater.*, 2020, 32, 2430–2439.
- 44 S. B. Naghadeh, B. Luo, Y.-C. Pu, Z. Schwartz,
 W. R. Hollingsworth, S. A. Lindley, A. S. Brewer,
 A. L. Ayzner and J. Z. Zhang, Size Dependence of Charge
 Carrier Dynamics in Organometal Halide Perovskite

Nanocrystals: Deciphering Radiative Versus Nonradiative Components, J. Phys. Chem. C, 2019, 123, 4610-4619.

Research Article

- 45 A. Kausar, A. Sattar, C. Xu, S. Zhang, Z. Kang and Y. Zhang, Advent of Alkali Metal Doping: A Roadmap for the Evolution of Perovskite Solar Cells, Chem. Soc. Rev., 2021, **50**, 2696.
- 46 J. Duan, Y. Zhao, X. Yang, Y. Wang, B. He and Q. Tang, Lanthanide Ions Doped CsPbBr₃ Halides for HTM-Free 10.14%-Efficiency Inorganic Perovskite Solar Cell with an Ultrahigh Open-Circuit Voltage of 1.594 V, Adv. Energy Mater., 2018, 8, 1802346.
- 47 J. Xu, J.-B. Liu, B.-X. Liu, J. Wang and B. Huang, Defect Engineering of Grain Boundaries in Lead-Free Halide Double Perovskites for Better Optoelectronic Performance, Adv. Funct. Mater., 2019, 29, 1805870.
- 48 W. Zhou, J. Fan, J. Luo, L. Lin, J. Zhou, J. Zhang, Z. Zhu and X. Zhang, Structural Confinement and Energetic Matching Synergistic Effect toward a High-Energy Transfer Efficiency and a Significant Red Emission Enhancement in a Eu²⁺, Ln³⁺ Co-doped Sr₉LiMn(PO₄)₇ Whitlockite Phosphor, Inorg. Chem., 2022, 61, 8767-8781.
- 49 K. Elzbieciak-Piecka, M. Suta and L. Marciniak, Structurally induced tuning of the relative sensitivity of LaScO3:Cr3+ luminescent thermometers by co-doping lanthanide ions, Chem. Eng. J., 2021, 421, 129757.
- 50 Q. Meng, L. Zhou, Q. Pang, X. He, T. Wei and J. Z. Zhang, Enhanced Photoluminescence of All-Inorganic Manganese Halide Perovskite-Analogue Nanocrystals by Lead Ion Incorporation, J. Phys. Chem. Lett., 2021, 12, 10204-10211.
- 51 S. Sarang, W. Delmas, S. Bonabi Naghadeh, V. Cherrette, J. Z. Zhang and S. Ghosh, Low-Temperature Energy

- Transfer via Self-Trapped Excitons in Mn(2 +)-Doped 2D Organometal Halide Perovskites, J. Phys. Chem. Lett., 2020, 11, 10368-10374.
- 52 J.-H. Wei, J.-F. Liao, X.-D. Wang, L. Zhou, Y. Jiang and D.-B. Kuang, All-Inorganic Lead-Free Heterometallic Cs₄MnBi₂Cl₁₂ Perovskite Single Crystal with Highly Efficient Orange Emission, Matter, 2020, 3, 892-903.
- 53 T. Cai, J. Wang, W. Li, K. Hills-Kimball, H. Yang, Y. Nagaoka, Y. Yuan, R. Zia and O. Chen, Mn²⁺/Yb³⁺ Codoped CsPbCl₃ Perovskite Nanocrystals with Triple-Wavelength **Emission** for Luminescent Solar Concentrators, Adv. Sci., 2020, 7, 2001317.
- 54 J. Luo, X. Wang, S. Li, J. Liu, Y. Guo, G. Niu, L. Yao, Y. Fu, L. Gao, Q. Dong, C. Zhao, M. Leng, F. Ma, W. Liang, L. Wang, S. Jin, J. Han, L. Zhang, J. Etheridge, J. Wang, Y. Yan, E. H. Sargent and J. Tang, Efficient and stable emission of warm-white light from lead-free halide double perovskites, Nature, 2018, 563, 541-545.
- 55 D. Wu, L. Liu, H. Liang, H. Duan, W. Nie, J. Wang, J. Peng and X. Ye, LiBAlF₆:Cr³⁺ (B = Ca, Sr) Fluoride Phosphors with Ultra-broad Near-infrared Emission for NIR pc-LEDs, Ceram. Int., 2022, 48, 387-396.
- 56 X. Li, Y. Wu, S. Zhang, B. Cai, Y. Gu, J. Song and H. Zeng, CsPbX₃ Quantum Dots for Lighting and Displays: Room-Temperature Synthesis, Photoluminescence Superiorities, Underlying Origins and White Light-Emitting Diodes, Adv. Funct. Mater., 2016, 26, 2435-2445.
- 57 H. Yu, J. Chen, R. Mi, J. Yang and Y.-G. Liu, Broadband Near-infrared Emission of K₃ScF₆:Cr³⁺ Phosphors for Night Vision Iimaging System Sources, Chem. Eng. J., 2021, 417, 129271.